American Journal of Biomedical and Life Sciences
2021; 9(6): 307-314
http://www.sciencepublishinggroup.com/j/ajbls
doi: 10.11648/j.ajbls.20210906.17
ISSN: 2330-8818 (Print); ISSN: 2330-880X (Online)

Finite Element Modeling for Fluorescence Molecular Tomography

Zhaolu Zuo[1], Shaobin Dou[1, *], Deyi Kong[1, 2], Kai Wu[1]

[1]Hefei Institutes of Physical Science, Chinese Academy of Sciences, Hefei, China

[2]Innovation Academy for Seed Design, Chinese Academy of Sciences, Bejing, China

Email address:
dsb@mail.ustc.edu.cn (Shaobin Dou)

[*]Corresponding author

To cite this article:
Zhaolu Zuo, Shaobin Dou, Deyi Kong, Kai Wu. Finite Element Modeling for Fluorescence Molecular Tomography. *American Journal of Biomedical and Life Sciences*. Vol. 9, No. 6, 2021, pp. 307-314. doi: 10.11648/j.ajbls.20210906.17

Received: October 25, 2021; **Accepted**: November 23, 2021; **Published**: November 24, 2021

Abstract: Non-contact Fluorescence Molecular Tomography (FMT) and Bioluminescence Tomography (BLT) has attracted more and more attention due to its unique advantages. For real experiments, how to obtain the 3D model of an object and the surface fluorescence distribution is one of the main obstacles. In this paper, an effective method to obtain the Finite Element Model is presented. We discuss the geometric and mathematical principles in detail. We prove that the FEM model generated by the method has enough quality for reconstruction. We demonstrate the quality of the model through a series of examples. This method can realize the whole process only by using a single-mode optical system. Firstly, a series of white light and fluorescence images are collected along the object in white light flat field illumination mode and excitation fluorescence mode respectively. The white light illumination images are used to reconstruct the 3D model contour of the object. After voxelization with appropriate resolution, we use the Delaunay algorithm to divide the model into tetrahedral finite elements. For the fluorescence image, we proposed a method based on vertex normal vector to realize the photon flux density mapping from 2D fluorescence image to 3D Finite Element Method (FEM) mesh nodes of the surface. The experimental results prove the accuracy of the model and the mapping, and the FEM obtained can meet the needs of FMT/ BLT reconstruction.

Keywords: FMT, BLT, 3D Modeling, FEM

1. Introduction

Optical molecular imaging can detect the macroscopic state of a living organism in terms of specific molecular activities in biological tissue, cellular, and subcellular levels by probing the fluorescence photons emitted from targeted molecular probes, which reflect the biochemical processes of living organisms in physiology and pathology [1, 2]. Fluorescence molecular imaging is carried out by injecting a certain specific molecular targeting probe. Then, the fluorescent molecular probe will bind to specific targets specifically. Through external excitation or biochemical reaction process, the molecular probe releases fluorescence photons. The photons transmitting through the tissue are detected by high-sensitivity detectors. After a 3D reconstruction, the distribution of fluorescent probes can be further obtained. As a valuable molecular imaging technology, fluorescence imaging has many unique advantages, such as high sensitivity, low price, no radiation, and convenience, which has been attracting more and more attention and applied in many fields [3-6]. In recent years, BLT [7-9] and FMT [11, 12] has become research focuses due to their excellent performance and made significant progress. Now, most of them are based on diffusion equation. The methods for solving the equation can be divided into 2 categories: analytical method and numerical method. The analytical methods are only suitable for solving the problems under some special conditions. The finite element methods can be applied to mose of complex situation, so it has been widely used. For the finite element method of FMT/BLT, the basic steps are as follows: (i) obtaining the 3D contour or structure of the object, (ii) generating finite element mesh, (iii)

mapping the flux density from the fluorescence image to finite element mesh nodes of the model surface, and (iv) establishling equations and solving it. In the above steps, obtaining an accurate FEM is the a critical step, which is related to the accuracy of the reconstruction results directly. However, most studies are based on artificial digital model or finite element model obtained by CT [13-15].

In this study, the object was illuminated by diffuse white light and excited by a laser. In these 2 modes, 36 images are captured respectively. For the white light images, we use the voxel carving method to reconstruct the 3D shape of the object and deploy the Delaunay algorithm to form tetrahedral finite elements. We propose a method based on a projection matrix to realize luminous flux density mapping of the model surface nodes from the fluorescence images sequence. The experiment results show that the proposed method can obtain the FEM for FMT effectively.

2. Experimental

2.1. Experiment Setup

The schematic of the experimental setup is shown in Figure 1. The projective geometry is shown in Figure 2. It is composed of a rotating platform, white light illumination source, laser excitation source, and deep cooling fluorescent camera. The rotating platform is driven by the stepper motor and has an accurate reset position as the start point of image acquisition. The target object is placed on the rotating platform and kept in the center position as far as possible. Adjust the camera focus so that the image can show the outline of the object clearly. The distance and angle between the camera and the rotating platform are adjusted so that the object is located in the center of the image and nearly fills the whole image area. In this way, we can ensure that the object does not exceed the visible area at any angle, and the image has more effective pixels. From the perspective of projection geometry, the intersection of camera's field of view of all angles contains the 3D space occupied by the object. The camera collects images along the circumference of the object. Before each image acquisition, the device should be reset to eliminate the accumulated error. In this experiment, a total of 36 images were captured from the start position with an interval of 10 degrees.

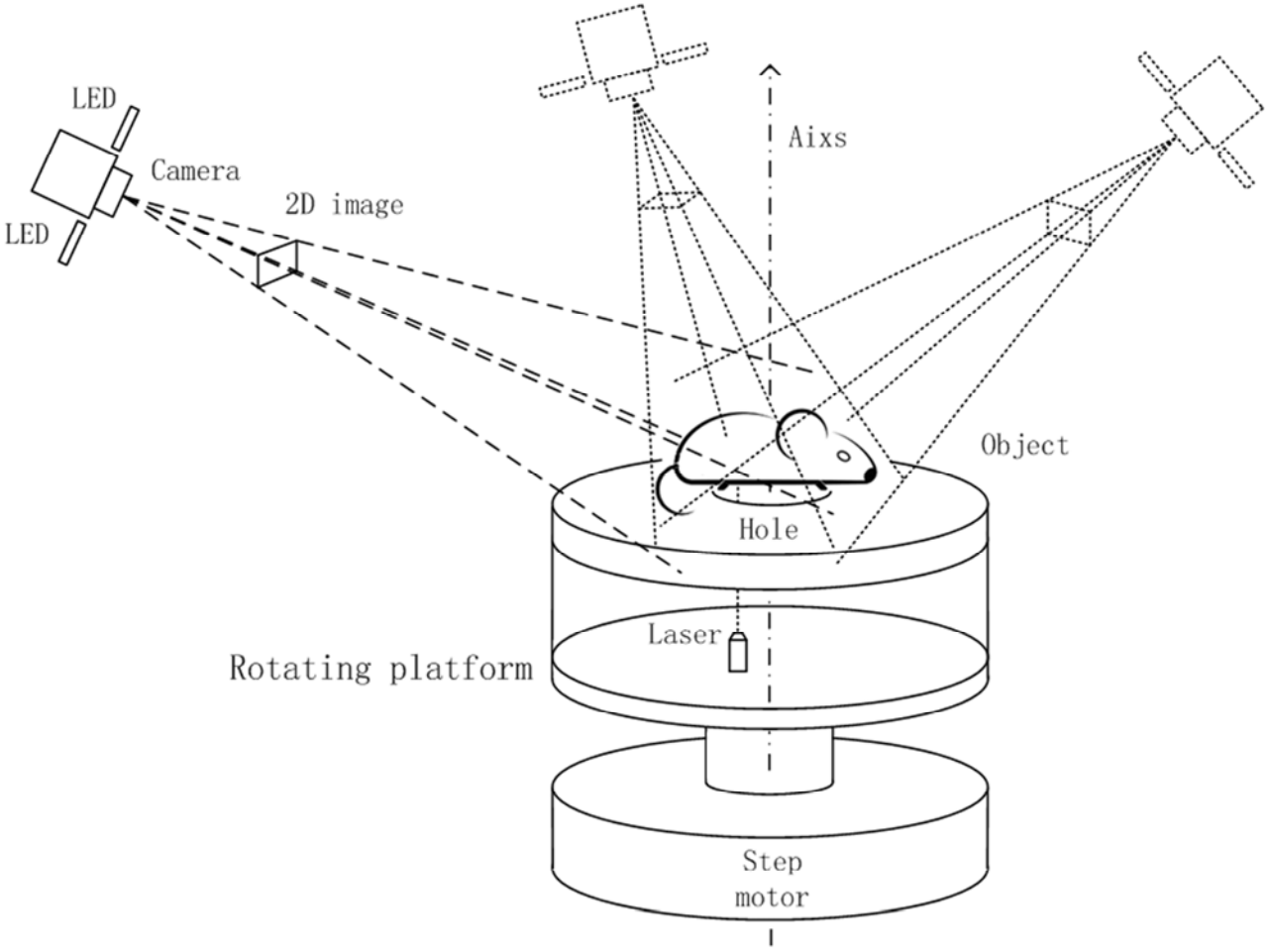

Figure 1. *The structure of fluorescence imaging system.*

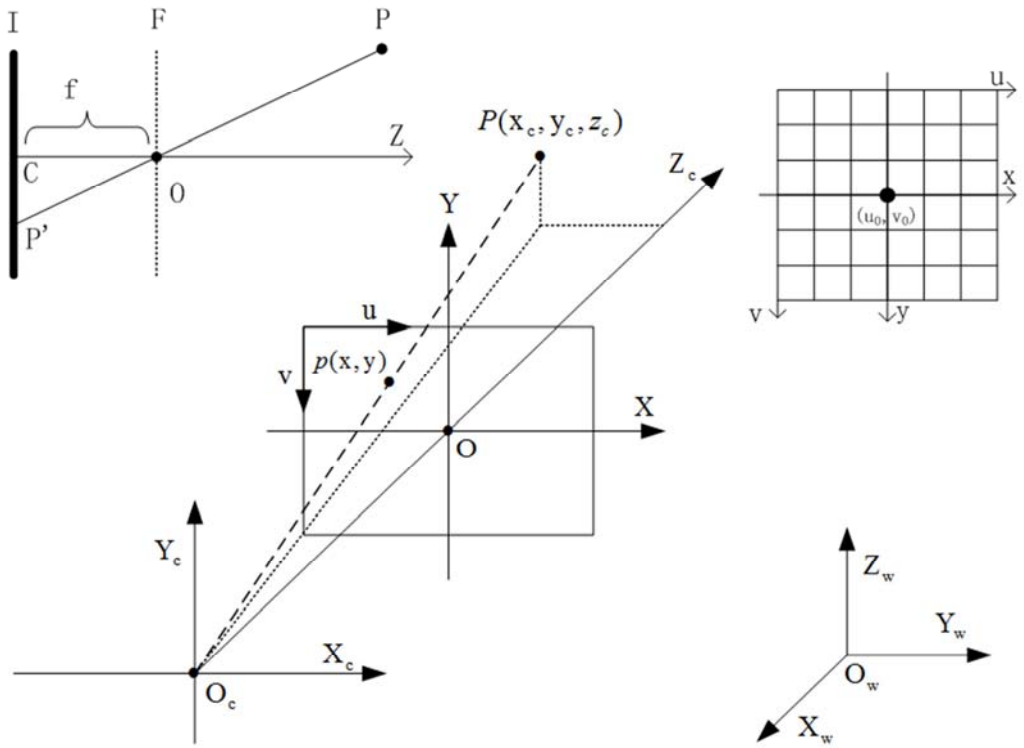

Figure 2. *The projective geometry.*

Before each acquisition, the rotating platform is reset once to ensure that the calibrated projection matrix can be used to project the image. The white light image and fluorescence image of mice are shown in Figure 3.

Figure 3. *(a) White light illumination image. (b) Fluorescence image.*

2.2. Projection Transformation

To simplify the calculation, the pinhole camera is used as the system model here, as shown in Figure 2. The I is the image plane, O is the focus, Z is the principal axis, and F is the focal plane. The *P* and *P′* are a point in the real world and the corresponding projection point respectively. In order to obtain the projection parameters, we use the Zhang Zhengyou calibration method to calibrate the system [10]. The chessboard calibration board is horizontally placed on the rotating platform and photographed every 10 degrees, and a total of 36 images are collected. Then, the calibration is carried out. When finishing, the internal parameter matrix In and the external parameter matrix Ex are got. The projection matrix P can be constructed:

$$P = In \cdot Ex \tag{1}$$

The projection from a real-world point to the camera sensor goes through the transformation of the world coordinate system, camera coordinate system, image coordinate system, and pixel coordinate system, respectively. The world coordinate is a 3D rectangular coordinate system, which describes the spatial position of the camera and the object, as shown in the lower right corner of Figure 2. The world coordinate system can be set freely according to the needs. The camera coordinate system takes the optical center of the camera as the origin, the Z-axis coincides with the optical axis and takes the shooting direction as the positive direction. The image coordinate system describes the projection and transmission relationship of objects from the camera coordinate to the image coordinate. The pixel coordinate system describes the arrangement of the camera sensor pixels. Its origin is located in the top left corner of the image. The transformation from world coordinate system to camera coordinate system is a mapping of 3D point to 3D point, involving external parameters [R, t]. The relationship of the world coordinate system and the camera coordinate system can be expressed as:

$$\begin{bmatrix} X_c \\ Y_c \\ Z_c \\ 1 \end{bmatrix} = \begin{bmatrix} R & T \\ \vec{0} & 1 \end{bmatrix} \begin{bmatrix} X_w \\ Y_w \\ Z_w \\ 1 \end{bmatrix} = \begin{bmatrix} r_{11} & r_{12} & r_{13} & t_{11} \\ r_{21} & r_{22} & r_{23} & t_{21} \\ r_{31} & r_{32} & r_{33} & t_{31} \\ 0 & 0 & 0 & 1 \end{bmatrix} \begin{bmatrix} X_w \\ Y_w \\ Z_w \\ 1 \end{bmatrix} \tag{2}$$

Here, (X_C, Y_C, Z_C) and (X_W, Y_W, Z_W) are the coordinates of

the point P in the camera coordinate system and the world coordinate system, respectively.

The transformation from camera coordinate system to image coordinate system is the projection from a point of 3D space to 2D space:

$$\begin{bmatrix} x \\ y \\ 1 \end{bmatrix} = \frac{1}{Z_c}\begin{bmatrix} f \cdot X_c \\ f \cdot Y_c \\ Z_c \end{bmatrix} + \begin{bmatrix} x_0 \\ y_0 \\ 0 \end{bmatrix} = \frac{1}{Z_c}\begin{bmatrix} f & 0 & x_0 & 0 \\ 0 & f & y_0 & 0 \\ 0 & 0 & 1 & 0 \end{bmatrix}\begin{bmatrix} X_c \\ Y_c \\ Z_c \\ 1 \end{bmatrix} \quad (3)$$

Where, (XC, YC, ZC) is the coordinate of point P in the camera coordinate system. (x, y) is the coordinate of the projection point P' in the image coordinate system. (x0, y0) is the offset of the main point.

The transformation from image coordinate system to pixel coordinate system is a mapping from the coordinate of real size to pixel coordinate, and it can be expressed as:

$$\begin{bmatrix} u \\ v \\ 1 \end{bmatrix} = \begin{bmatrix} 1/dx & 0 & u_0 \\ 0 & 1/dy & v_0 \\ 0 & 0 & 1 \end{bmatrix}\begin{bmatrix} x \\ y \\ 1 \end{bmatrix} \quad (4)$$

The (u, v) is the coordinate of the projection point in the pixel coordinate system, dx and dy represent the number of pixels in the X and Y directions of the camera sensor, respectively. (u_0, v_0) is the center of the pixel plane.

To sum up, we can get the mapping relationship from the world coordinate system to the pixel coordinate system:

$$\begin{bmatrix} u \\ v \\ 1 \end{bmatrix} = \frac{1}{Z_c}\begin{bmatrix} f/dx & 0 & u_0 & 0 \\ 0 & f/dy & v_0 & 0 \\ 0 & 0 & 1 & 0 \end{bmatrix}\begin{bmatrix} R & T \\ 0 & 1 \end{bmatrix}\begin{bmatrix} X_w \\ Y_w \\ Z_w \\ 1 \end{bmatrix} = \frac{1}{Z_c} \cdot In \cdot Ex \begin{bmatrix} X_w \\ Y_w \\ Z_w \\ 1 \end{bmatrix} = \frac{1}{Z_c} \cdot P \cdot \begin{bmatrix} X_w \\ Y_w \\ Z_w \\ 1 \end{bmatrix} \quad (5)$$

Here, the P is the projection matrix created by calibration.

2.3. 3D Surface Reconstruction

In the reconstruction of FMT/BLT, we must obtain the 3D surface model of the object and the distribution of fluorescence, and then various reconstruction algorithms can be implemented. Usually, the 3D structure of the object is obtained through XCT scanning. However, XCT scanners are not always available due to the radiation and high price. Even if 3D information is obtained by XCT, how to realize the surface fluorescence distribution through fluorescence image is also a challenge.

In this study, we propose a 3D surface modeling method based on sequence images, which calculates the contour of the object through the projection matrix and spatial pixel consistency, and then maps the 2D fluorescence image to the 3D model surface through the same matrix. It should be noted that due to using an optical method, the internal structure of the object cannot be obtained. It is assumed that the object is homogeneous. The experimental results show that in high scattering tissue, this assumption does not cause obvious errors in the subsequent reconstruction results. We take two series of images in white light mode and fluorescent mode, respectively. The white light image is used to generate the model surface of the object. Under white illumination, the mouse surface can be regarded as a Lambert light source. Generally, deep cooled fluorescent cameras are monochromatic and can only capture high-quality gray images. In this case, color information cannot be used in the surface reconstruction. Considering these constraints, we propose an Improved Space Voxel Carving algorithm based on pixel value consistency to generate the 3D surface model of the object.

In this method, the intersection of the camera's field of view at all snapping angles is taken as the target space, and then the image series are back-projected to eliminate the voxels beyond the two-dimensional contour. In fact, this is to calculate the intersection of 3D cones of all contour image back projections. Experiments show that when there are enough images, the 3D model of the object is an effective approximation of the real object.

The specific steps of this method are as follows: (i) at each shooting position, the system is calibrated to obtain projection matrixes, (ii) obtain the contour of the object, (iii) calculate the 3D space by the FOV intersection of each shooting position, (iv) project each voxel onto every image, (vi) if the projection values are equal, the voxel is retained, otherwise, rejected, and (v) smooth the surface. Through the above steps, the final 3D model of the object can be obtained.

In the experiment, the background is made of black material with high absorbance. Under the illumination of uniform white light, the background and the target object have obvious brightness distinctions, which can be separated through the threshold simply. To improve the reconstruction effect, we also do some post-processing, such as removing some small non-connected areas and filling the holes in the contour.

2.4. Finite Element Segmentation

In scientific calculation and engineering applications, it is sometimes difficult to obtain the exact solution to the problem. So, the Finite Element Method (FEM) is usually employed to obtain the approximate solution. In FEM, the solution domain is usually divided into a large number of small elements. The quality and quantity of the finite element affect the quality and stability of the result directly. There are many mesh generation algorithms, but most of them are only good at one aspect. The sort of front technique is a heuristic algorithm, which is easy to generate mesh with arbitrary granularity and has good quality tetrahedral meshes near the external surfaces, but the stability is not easy to obtain in 3D geometries [23-25]. The Advancing Front Techniques [26-31], Delaunay-based methods [32-37] and Octree-basedmethods [16-19], etc., has its own advantages and can produce good results under certain conditions. The sort of Delaunay-based methods can divide an entity into tetrahedrons, which is represented by arbitrarily distributed vertices. Also, it can be applied to complex situations. One of the drawbacks is that they can't deal with concave and internal surfaces. For the 3D model generated by space curving technology, there is no concave outside and no internal holes or inner surface. The Delaunay method has theoretical guarantee of correctness, which can handle complex 3D geometries fastly. In this paper, we choose the Delaunay

method to generate the tetrahedral finite element mesh. As the simplicity and efficiency, 4-noded meshes have been selected for computing. The Tetgen [38] is a free program, which can generate tetrahedral meshes for any 3D polyhedral domains following the Delaunay criterion. It also provides a variety of optional features to improve the quality of mesh generation. It is suitable for numerical different computation, such as finite volume and Finite Element methods. Here, we use the Tetgen to generate tetrahedral meshes. The finite element mesh of a cylindrical phantom is shown in Figure 4.

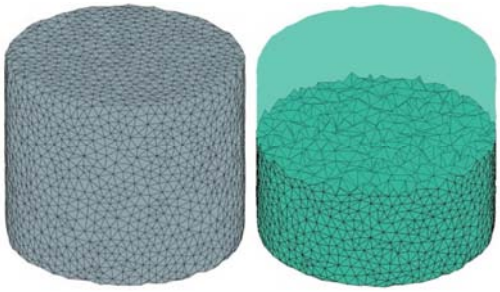

Figure 4. *Surface triangular mesh and inner tetrahedral mesh of a cylindrical phantom.*

2.5. Flux Density Mapping of Fluorescent Photons

The value of the surface nodes is one of the necessary conditions for the FMT/BLT reconstruction. The accuracy of the value is directly related to the quality of reconstruction. For animals, it can be considered that the surface is a Lambert source. A Lambertian surface has uniform diffusion. Its radiance is the same in all directions. That is to say, the brightness of the surface radiation has nothing to do with the direction. According to Lambert's cosine law, the radiation intensity emitted from the surface unit area in a particular direction is proportional to the cosine of the angle between the direction and the surface normal. The relationship can be expressed as follows:

$$I_\theta = I_N \cos\theta \tag{6}$$

here, I_N is the luminous intensity in the vector direction perpendicular to the surface of the object, and I_θ is that of angle θ.

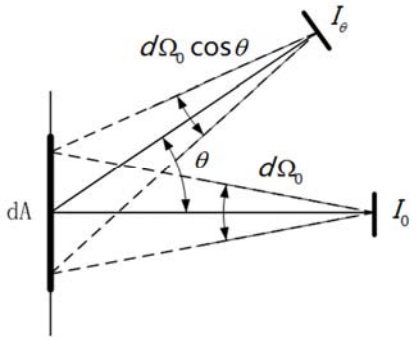

Figure 5. *The relationship between the radiation intensity and the angle.*

The value of the surface nodes of the FEM can not be obtained directly. It must to be mapped from 2D fluorescent photos. Here, we propose a flux density mapping method based on minimum angle and cosine principle. In the mapping, the image with the smallest angle between the optical axis and the normal vector is selected as the source. According to the coordinates of a node and the corresponding projection matrix, the projection points of the node are calculated, and then the luminous flux of the node can be obtained. Usually, a node is shared by multiple faces and its value is calculated multiple times. In this case, the average value is taken as the final value of the node. The detailed process is as follows:

(i) Calculate the normal vector $N_m(x_m, y_m, z_m)$ of the surface triangular mesh and the normal vector $N_c(x_c, y_c, z_c)$ of the camera plane,

$$\begin{Bmatrix} x_c \\ y_c \\ z_c \end{Bmatrix} = R^{'} \bullet K^{-1} \begin{Bmatrix} u/2 \\ v/2 \\ 1 \end{Bmatrix} \tag{7}$$

here, R is the rotation matrix of the camera, K is the internal parameter matrix of the camera, and u and v are the width and height of the image in pixels.

(ii) Calculate the angle θ between the normal vector of triangle mesh and optical axis of the camera,

$$\theta = \begin{cases} \text{acos}\left((N_{\text{cam}}.N_{\text{face}})/|N_{\text{cam}}|.|N_{\text{face}}|\right), S \geq 0 \\ 2\pi\text{-acos}\left((N_{\text{cam}}.N_{\text{face}})/|N_{\text{cam}}|.|N_{\text{face}}|\right), S < 0 \end{cases} \tag{8}$$
$$S = N_{\text{cam}} \times N_{\text{face}}$$

As the range of arccosine is [0, π], it is necessary to determine whether the included angle is in the range. Here, This is done by calculating the sign of the cross product of two vectors. Then, the image with the smallest angle is selected as the mapping target.

(iii) Get the average mapping values of all surface triangular mesh nodes according to Lambert's cosine law.

The results of surface luminous flux density mapping of the object model are shown in Figure 6. It can be seen that the fluorescence distribution of the model is consistent with the actual object.

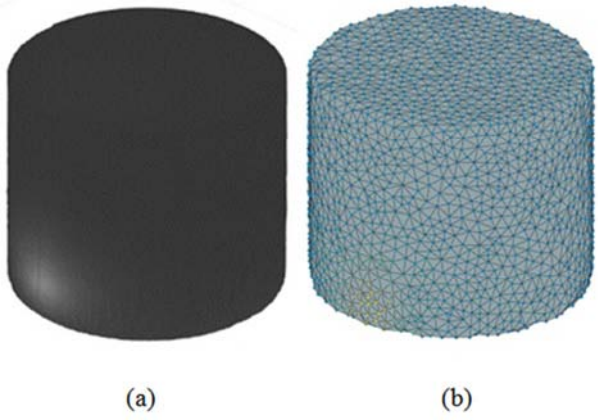

Figure 6. *The result of surface flux density mapping. (a) Surface view mode. (b) Mesh view mode.*

3. Results and Discussion

3.1. The Accuracy of Contour Reconstruction

To measure the accuracy of the algorithm, we use four kinds of phantoms for testing. These models are regular columnar body with sections of triangle, quadrangle, pentagon, hexagon, and circle, as shown in the 1st line of Figure 6 for each phantom, white light illumination images of 36 angles were uniformly captrued for 3D contour reconstruction. The section image of the reconstructed model is in the 2nd line of Figure 5. The image size is marked by the bounding box. Comparing the actual measured object size, the modeling error of each model is obtained, as shown in the 3rd line of Figure 7.

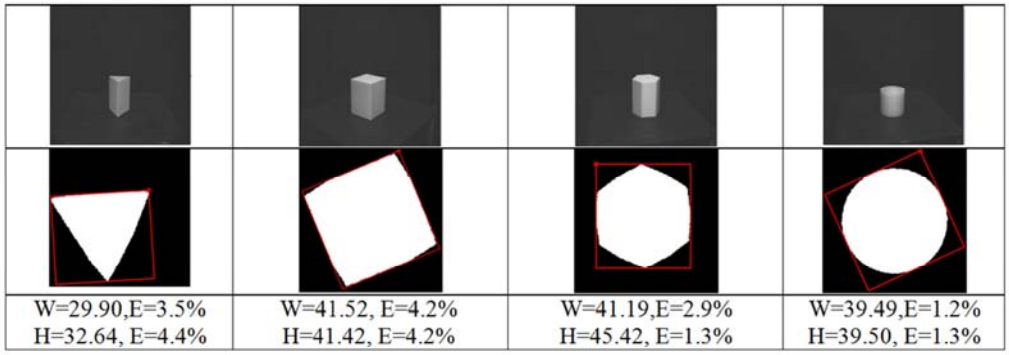

Figure 7. *The phantom reconstruction size error of different shapes. The W, H and E are abbreviations for Width, Height and Error respectively.*

It can be seen that the proposed algorithm has very high modeling accuracy, and the average error is less than 0.8%. The more images involved, the better the quality of the model. If the accuracy of calibration and the quality of the image are further improved, the error can be further reduced.

3.2. Luminous Flux Density Mapping Accuracy

The accuracy of surface node luminous flux density includes position accuracy and brightness accuracy. The mapping adopts the same method as the surface reconstruction, so they have the same position accuracy, which has been evaluated above. Here, only the accuracy of brightness value mapping is evaluated. We take the projection points values of some nodes on the fluorescence image and compare them with the values of the nodes themselves. One of the nodes is shown in Figure 8.

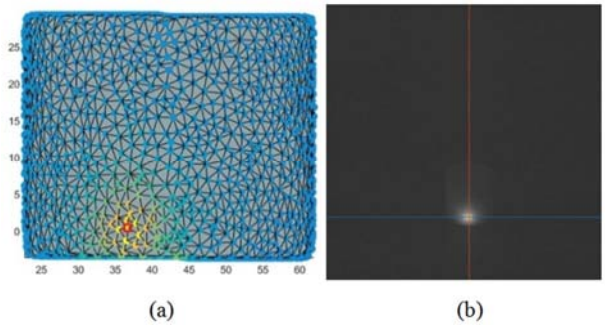

Figure 8. *Accuracy evaluation of flux mapping of surface mesh node. (a) The flux intensity value of the surface mesh node. (b) Corresponding pixel value of object surface.*

We take 8 node values on the FEM model surface and the pixel values of the projection points of the fluorescence image. These points cover the range from the maximum value to the minimum value. The comparison results are shown in Table 1.

Table 1. *The evaluation of FEM surface node value error.*

node coordinates	Node number	Node value	Pixel value	Error
56.03, 36.81, 0.39	2283	199	171	14.01%
55.57, 35.59, 0.16	2244	184	178	3.26%
55.36, 35.17, -1.53	2225	155.3	172	10.75%
56.08, 36.93, 3.61	2289	145.4	133	8.53%
56.75, 40.61, 0.66	2384	126	126	0.00%
56.79, 44.62, 14.05	2394	60	58	3.33%
54.67, 33.22, 22.16	2180	57.5	55	4.35%
55.39, 50.11, 11.21	2227	56.67	57	0.58%

It can be found that the errors increase with the node value. This is because the high brightness area of the fluorescent image is usually smaller. Due to the error of the reconstricted model, the mapping position of the surface node may fall into the larger dark area. The two kinds of errors above are related to the quality of the image, the projection matrix accuracy, and the quality of the contour model, etc. Improving these factors can further make better the quality of contour reconstruction and the accuracy of surface flux density mapping.

4. Conclusion

For FMT, it is a crucial step to obtain the 3D calculation model of the object and realize the mapping of luminous flux density from fluorescence images to the model surface, accurately. In this paper, a method to obtain the FEM using a single-mode optical system is proposed and discussed in detail. The white light images are used to obtain the 3D contour model of the object. After the finite element segmentation, the fluorescence images are used to map the flux density of the surface nodes. Here, we adopt the back projection space carving method to reconstruct the 3D contour of the object. Then, the Delaunay method is used to

segment the model. For the flux density mapping, we proposed a method based on the product of the normal vectors to find out the image with the smallest angle as the mapping source. By using the same projection matrix and the same method, the problem of registration is avoided completely. Experiment results show that the proposed method can accurately obtain the FEM of the object and realize flux density mapping. As the photon energy of visible light is so weak, it usually can't penetrate the object directly, this method can only get the external contour. In the reconstruction, we assume that the object is homogeneous, which will affect the accuracy of the reconstruction results to some extent. However, the experiments show that this assumption has little influence in a highly scattering medium.

This paper presents a new algorithm, which can obtain FEM accurately by using a single-mode imaging system. Compared with other multi-mode methods, our scheme has unique advantages. The research of this paper solves a key problem of finite element solution in FMT / BLT, and has great significance.

Funding and Disclosures

The research in this paper has been funded by the Key research and development plan of Anhui Province (202004a05020033) and the Science and technology plan of Lianyungang high tech Zone (CX201906).

References

[1] Vls K K, Kjelgaard-Hansen M, Ley C D, et al. In vivo fluorescence molecular tomography of induced haemarthrosis in haemophilic mice: link between bleeding characteristics and development of bone pathology. BMC Musculoskeletal Disorders, 21: 1 (2020).

[2] Meng H, Gao Y, Yang X, et al. K-nearest Neighbor Based Locally Connected Network for Fast Morphological Reconstruction in Fluorescence Molecular Tomography. IEEE Transactions on Medical Imaging, 99: 1-1 (2020).

[3] V. Ntziachristos, J. Ripoll, L. V. Wang, and R. Weissleder, Looking and listening to light: the evolution of whole-body photonic imaging, Nat. Biotechnol. 23, 313-320 (2005).

[4] B. W. Rice, M. D. Cable, and M. B. Nelson, In vivo imaging of light-emitting probes, J. Biomed. Opt. 6, 432-440 (2001).

[5] Strangman, Gary, D. A. Boas, and J. P. Sutton, Non-invasive neuroimaging using near-infrared light, Biological Psychiatry 52, 679-693 (2002).

[6] Dianwen Zhu, Yue Zhao, Reheman Baikejiang, Zhen Yuan, and Changqing Li. Comparison of regularization methods in fluorescence molecular tomography. Photonics, 1 (2): 95–109 (2014).

[7] L. Yin, K. Wang, T. Tong, Q. Wang, J Tian, Adaptive Grouping Block Sparse Bayesian Learning Method for Accurate and Robust Reconstruction in Bioluminescence Tomography. IEEE Transactions on Biomedical Engineering, 99, 1-1 (2021).

[8] Wang G, Li Y, Jiang M. Uniqueness theorems in bioluminescence tomography. Medical Physics. 31 (8), 2289-2299 (2004).

[9] Feng JC, Jia KB, Yan GR, et al. An optimal permissible source region strategy for multispectral bioluminescence tomography. Optics Express. Sep 29, 16 (20), 15640-15654 (2008).

[10] Zhang Z. A Flexible New Technique for Camera Calibration. IEEE Transactions on Pattern Analysis and Machine Intelligence, 22 (11), 1330-1334 (2000).

[11] H Wang, Bian C, Kong L, et al. A Novel Adaptive Parameter Search Elastic Net Method for Fluorescent Molecular Tomography. IEEE Transactions on Medical Imaging, p. 99 (2021).

[12] Ntziachristos, Vasilis, et al. "Fluorescence molecular tomography resolves protease activity in vivo." Nature Medicine 8.7, 757-761 (2002).

[13] Cong A X, Wang G. A finite-element-based reconstruction method for 3D fluorescence tomography. Optics Express, 13 (24): 9847-9857 (2005).

[14] Chen D, Liang J, Yao L, et al. A Sparsity-Constrained Preconditioned Kaczmarz Reconstruction Method for Fluorescence Molecular Tomography [J]. BioMed Research International, 2016: 1-15 (2016).

[15] A. Ale, V. Ermolayev, E. Herzog, C. Cohrs, M. H. de Angelis, and V. Ntziachristos, FMT-XCT: in vivo animal studies with hybrid fluorescence molecular tomography-X-ray computed tomography, Nat Methods 9, 615-U140 (2012).

[16] M. Saxena, P. M. Finnigan, C. M. Graichen, A. F. Hathaway, and V. N. Parthasarathy. Octree-based automatic mesh generation for nonmanifold domains. Engineering with Computers. 11, 1–14 (1995).

[17] M. S. Shephard and M. K. Georges. Three-dimensional mesh generation by finite octree technique. International Journal for Numerical Methods in Engineering, 32, 709–749 (1991).

[18] K. Tchon, K. Mohammed, G. Francois, C. Ricardo, Constructing anisotropic geometric metrics using octrees and skeletons, in: Proceedings of the 12th International Meshing Roundtable. p. 293–304 (2003).

[19] P. Frey, L. Marechal, Fast adaptive quadtree mesh generation, in: Proceedings of the Seventh International Meshing Roundtable. p. 211–222 (1998).

[20] Sevick EM, Lakowicz JR, Szmacinski H, Nowaczyk K, Johnson ML. Frequency domainimaging of absorbers obscured by scattering. Journal of photochemistry and photobiology. B, Biology. 16, 169-185 (1992).

[21] Martin WN. Aggarwal J K. Volumetric descriptions of objects from multiple views. IEEE Trans onPattern Analysis and Machine Intelligence, (1983).

[22] Qianqian Fang and David Boas, "Tetrahedral mesh generation from volumetric binary and gray-scale images," Proceedings of IEEE International Symposium on Biomedical Imaging. p. 1142-1145 (2009).

[23] R. Lohner. Progress in grid generation via the advancing front technique. Engineering with Computers. 12, 186–210 (1996).

[24] S. H. Lo. Volume discretization into tetrahedra-I. Verification and orientation of boundary surfaces. Computers and Structures. 39 (5), 493–50 0 (1991).

[25] R. Lohner, P. Parikh, and C. Gumbert. Interactive generation of unstructured grid for three dimensional problems. In Numerical Grid Generation in Computational Fluid Mechanics. (Pineridge Press, 1988), p. 687–697.

[26] C. Lee, Automatic metric advancing front triangulation over curved surfaces, Eng. Comput. 17, 48–74 (2000).

[27] R. Lohner, C. Juan, Generation of non-isotropic unstructured grids via directional enrichment, Internat. J. Numer. Methods Engrg. 49 (1), 219–232 (2000).

[28] S. Lo, Volume discretization into tetrahedra-I, Verification and orientation of boundary surfaces, Comput. Structures. 36, 493–500 (1991).

[29] R. Lohner, Progress in grid generation via the advancing front technique, Engrg. Comput. 12, 186–199 (1996).

[30] D. Marcum, N. Weatherill, Unstructured grid generation using iterative point insertion and local reconnection, AIAA J. 33 (9), 1625 (1995).

[31] K. Nakahashi, D. Sharov, Direct surface triangulation using the advancing front method, AIAA, p. 95-1686-CP (1995).

[32] Q. Du, D. Wang, Boundary recovery for three dimensional conforming Delaunay triangulation, Comput. Methods Appl. Mech. Engrg. 193, 2547-2563 (2004).

[33] Q. Du, D. Wang, Tetrahedral mesh generation and optimization based on centroidal Voronoi tessellations, Internat. J. Numer. Methods Engrg. 56, 1355–1373 (2003).

[34] X. Li, Sliver-free three dimensional Delaunay mesh generation, Ph.D thesis, (2000), UIUC.

[35] N. Weatherill, O. Hassan, Efficient three dimensional Delaunay triangulation with automatic point creation and imposed boundary constraints, Internat. J. Numer. Methods Engrg. 37, 2005-2039 (1994).

[36] Q. Du, D. Wang, Constrained boundary recovery for three dimensional Delaunay triangulation, Internat. J. Numer. Methods Engrg. 61, 1471–1500 (2004).

[37] P. George, Gamanic3d, adaptive anisotropic tetrahedral mesh generator, Technical Report, (2002), INRIA.

[38] Hang Si, TetGen, a Delaunay-based quality tetrahedral mesh generator, ACM Transactions on Mathematical Software. 41, 36 (2015).